



Elevating strength–ductility synergy in aluminum matrix composites by multiscale and dual-structured reinforcing particulates

Xuezheng Zhang^{1,2,3,a)}, Wenhao Lu^{1,2}, Tijun Chen^{1,2,a)}

¹State Key Laboratory of Advanced Processing and Recycling of Nonferrous Metals, Lanzhou University of Technology, Lanzhou 730050, China

²School of Material Science and Engineering, Lanzhou University of Technology, Lanzhou 730050, China

³Wenzhou Engineering Institute of Pump & Valve, Lanzhou University of Technology, Wenzhou 325105, China

a)Address all correspondence to these authors. e-mails: zhangxz@lut.edu.cn; chentj@lut.edu.cn

Received: 22 March 2023; accepted: 27 July 2023; published online: 11 August 2023

To elevate strength–ductility synergy in aluminum matrix composites, we propose a strategy of forming multiscale and dual-structured (M&D) reinforcing particulates, which are composed of nano-/submicro-particulates with monolithic structure ($< 2 \mu\text{m}$) and micro-particulates with core–shell (CS) structure ($> 2 \mu\text{m}$), and explore the effects of particulate fraction on microstructure and tensile properties. The results show that an increase in M&D particulate fraction decreases the grain size of Al matrix due to impeding of particulates against disappearance of grain boundary, and the tensile strengths increase significantly while the elongation first increases and then decreases. Comparatively, the synthesized M&D particulates in this work exhibit a much better toughening effect than CS particulates or traditional monolithic ones. Corresponding strengthening and toughening mechanisms are discussed from the perspective of strength contribution calculation, post-deformed transmission and scanning electron microscopy observations. This work would provide references for conquering the low ductility of metal matrix composites and promotes their widespread application in industry.

Introduction

Unlike particles in precipitation hardening, the most popular means of strengthening alloys, ceramic reinforcing particulates such as SiC, B₄C in aluminum matrix composites (AMCs) are stable at elevated temperatures, making AMCs attractive to high temperature applications [1–3]. However, the introduction of ceramic particulates into an aluminum matrix always leads to the reduction of ductility, which seriously limits the applications of the AMCs [4–6]. Plentiful efforts have been conducted to enhance the ductility of AMCs through, for instance, minimizing, homogenizing and/or spheroidizing the reinforcing particulates [7–11]. However, the effects are limited due mainly to the poor wettability of the reinforcing particulates by the matrix melt and therefore weak interfacial bonding between the matrix and the ceramic reinforcing particulates [1]. Replacement of ceramic particulates with in situ formed intermetallic compounds like Al₃Ti (or (Al, Si)₃Ti in some case [11]), Al₃Ni were also implemented recent years [12–14], in an attempt to reduce the severe ductility deterioration by improving interfacial

bonding strength between matrix and the particulates. However, the ductility of the resultant composites is still much lower than the corresponding Al matrix. For instance, the 356Al matrix composite reinforced with (Al, Si)₃Ti intermetallic particulates only exhibits a limited ductility of 3.1%, far away from the matrix alloy (8.6%) [15].

A strategy towards improving the strength–ductility synergy of AMCs was put forward in the past decade by replacing monolithic intermetallic particulates with core–shell structured (CS) ones, which were composed of inner metallic core (like Ti, Fe) and outer intermetallic shell (like Al₃Ti, Al₃Fe) [11, 16, 17]. The CS particulates could reduce the initial crack size by restraining it in the hard shell and constrain crack propagation by the soft metallic core, thus showing great superiority in improving the ductility of AMCs over the traditional monolithic ones. For example, the ductility of Ti@ (Al–Si–Ti) CS particulate-reinforced A356 composite (8.3%) was comparable to that of the matrix alloy (8.6%) [11]. Despite such an advance, the CS particulates, which are generally at

the microscale, exhibit a limited strengthening effect through mainly load transfer mechanism, such as 12.3% of strength increment in the above case [11]. Reducing the CS particulate size may be a good solution, but the aggravated difficulty in shell control with decreasing size makes it impossible to acquire CS particulates with much smaller size lower than 1 μm [18]. How to effectively elevate the strength–ductility synergy in metal matrix composites to widen their industrial application remains a big challenge.

Very recently the authors proposed a novel strategy to overcome the aforementioned dilemma by rendering multi-scale and dual-structured (M&D) architecture to the reinforcing particulates [19]. The M&D particulates consist of nano-/submicro- Al_3Ti reinforcing particulates with monolithic structure ($< 2 \mu\text{m}$) and micro-CS reinforcing particulates with inner Ti core and outer Al_3Ti intermetallic shell ($> 2 \mu\text{m}$) [19]. Through tailored successive deformation of reinforcing particulates at multiscale, a considerable strength enhancement as high as 65.1% and a decent ductility (21.8%) comparable to the pure Al matrix (22.9%) was simultaneously obtained in AMCs, which exhibits a much better effect of toughening than other kinds. However, only a fixed volume fraction of M&D reinforcing particulates was involved in that work and the presented mechanical properties were actually not the optimized ones. In other words, there is still room for property improvement from M&D reinforcing particulates. What's more, the strengthening mechanisms of the M&D reinforcing particulates remains unclear to date. Therefore, the M&D reinforcing particulates with varied volume fractions are synthesized in this study, and their effects on microstructure and tensile properties are systematically investigated. Additionally, the strengthening mechanisms of M&D reinforcing particulates

are quantified by calculating their respective strength contributions and the corresponding toughening mechanisms are also discussed.

Results

Uniform distribution of reinforcing particulates

The SEM microstructures and EPMA Ti element mappings of the 3%, 5%, 8% and 10% Ti_p AMCs are displayed in Fig. 1(a)–(h). It is clear that under the backscattered electron mode the reinforcing particulates with bright contrast distribute uniformly within the pure Al matrix with dark contrast, without distinct clusters of agglomerates. This indicates that the fabrication method utilized in this work is efficient in dispersing reinforcements in AMCs. Close-up SEM images further reveal that the reinforcing particulates of all AMCs consist of two kinds: monolithic particulates and CS particulates [Fig. 2(a)–(d)]. The former is much smaller in size, while the latter is much larger composed of outer Al–Ti intermetallics as well as inner Ti core [Fig. 2(e)]. Clearly, the formation of such dual-structured reinforcing particulates is related to the wide size distribution of original Ti powders that ranges from nanometer to micrometer. The Ti powders smaller than a critical value (about 2 μm) evolve completely into monolithic Al–Ti intermetallics, and the larger ones evolve partially into monolithic Al–Ti intermetallics to form the outside shell with the residual Ti becoming the inside Ti core. It is worthwhile noting that a smaller fraction ($< 1.2\%$) of voids exists in the synthesized AMCs [labelled by arrowhead in Fig. 2(a)–(d)], which is inevitable in the particulate-reinforced AMCs fabricated by powder metallurgy.

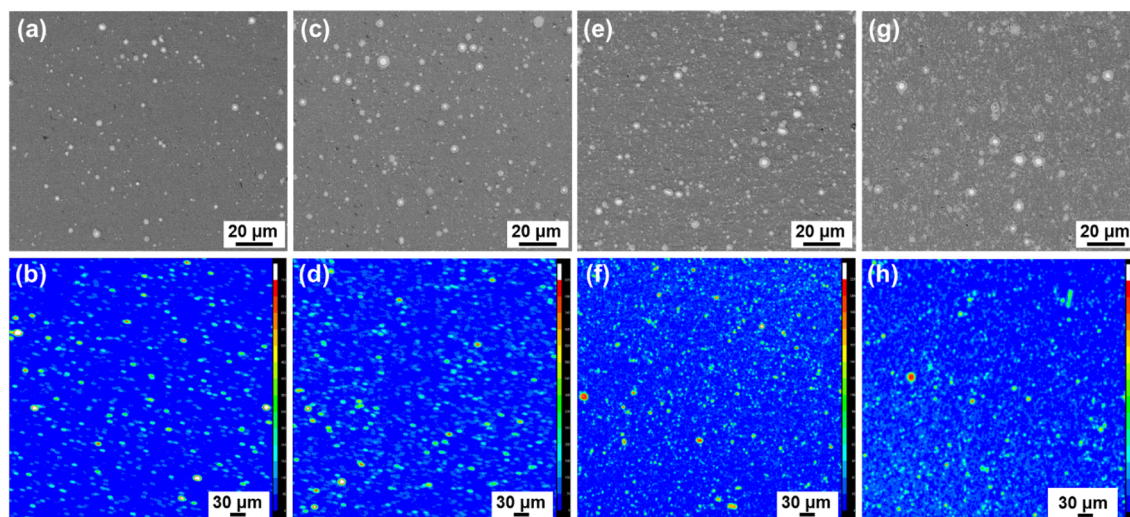


Figure 1: (a, c, e, g) SEM micrographs and (b, d, f, h) EPMA micrographs of (a, b) 3%, (c, d) 5%, (e, f) 8% and (g, h) 10% Ti_p AMCs.

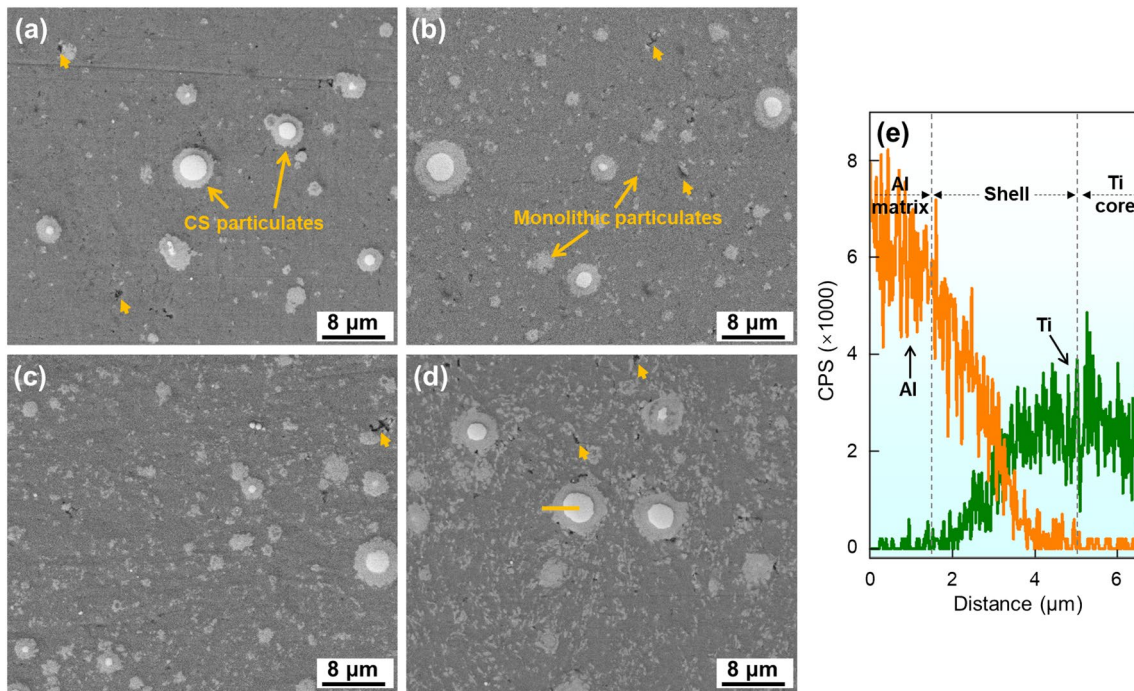


Figure 2: (a–d) Magnified SEM micrographs of (a) 3%, (b) 5%, (c) 8% and (d) 10% Ti_p AMCs, and (e) EDS element distribution of Al and Ti elements along the shell area marked by the line in (d).

Grain size and grain orientation distribution of Al matrix

EBSD characterization is performed to verify the difference in the grain size distribution and grain orientation of Al matrix in the different AMCs. As shown in Fig. 3(a)–(d), the grain size distribution determined from the EBSD inverse pole figures shows

that the average grain size of Al matrix reduces from 13.32 μm for the pure Al to 0.78 μm for 3% Ti_p AMCs, 0.73 μm for 5% Ti_p AMCs, 0.72 μm for 8% Ti_p AMCs and finally to 0.70 μm for 10% Ti_p AMCs [Fig. 3(e)–(h)]. That is, an increase in the reinforcement fraction decreases the grain size of Al matrix in the AMCs. This can be ascribed to the impeding of reinforcing particulates

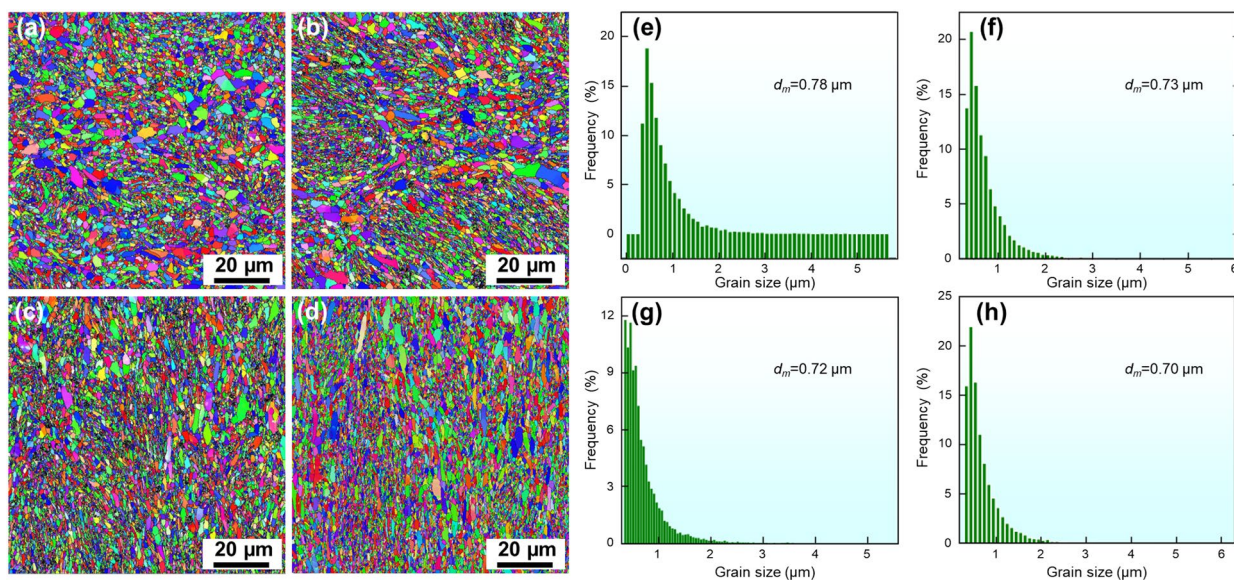


Figure 3: (a–d) EBSD inverse pole figures and (e–h) grain size distribution of Al matrix in (a, e) 3%, (b, f) 5%, (c, g) 8% and (d, h) 10% Ti_p AMCs.

against the disappearance of grain boundary. As shown in Supplementary Fig. S1(a) and (b), the grains labelled by letters “A” and “B” are undergoing mergence, but the mergence process is obviously delayed due to the existence of reinforcing particulates at the grain boundary (pointed by arrow). The uniform distribution of reinforcing particulates around the Al grain boundaries, as indicated in Supplementary Fig. S1(b), greatly postpones the overall grain growth through coalescence, and apparently the more fraction of the reinforcing particulates, the stronger the impeding effect and thus the smaller the average Al grain size [Fig. 3(e)–(h)]. That’s the way how the grain growth in different AMCs is restrained. However, in some grains certain amount of reinforcing particulates, especially those at the nanoscale, are incorporated into the grain interiors [circled by the dashed frame in Supplementary Fig. S1(b)], which is the results of complete mergence between the adjacent Al grains.

In addition, the results from EBSD pole figures of Al matrix indicate that there’s no distinct preferred grain orientation, i.e., texture, in all the synthesized AMCs [Supplementary Fig. S1(c)–(f)]. As the powder metallurgy method utilized in this work belongs to a “gentle” processing, after which less plastic deformation can be reserved in the microstructure along the forging direction, especially when compared with other severely-deformed techniques such as rolling [20], squeezing [21], etc. In addition, the difference between the grain orientation in the different AMCs is negligible, which might be ascribed to the fact that the processing parameters including ball milling, hot pressing and subsequent heating are all consistent. The absence of preferred grain orientation in the AMCs means that on one hand, there is no anisotropy in the tensile properties and therefore there’s no need to differentiate the direction along which the tensile properties are tested. On the other hand, the effect of texture strengthening can be neglected in analyzing the strengthening mechanisms that follows.

Size distribution of reinforcing particulates

TEM characterization along with EDS elemental mapping was further performed to identify the microstructures in different AMCs. As shown in Fig. 4(a)–(p), the distribution of reinforcing particulates at nanoscale and sub-microscale is still uniform in all the synthesized AMCs. Considering the uniform distribution of reinforcing particulates at microscale (Fig. 1), it can be concluded that the reinforcing particulates at multi-scale is considerably uniform in all the AMCs. Besides, with an increase in the fraction of reinforcing particulates, the proportion of reinforcements with larger size, especially these at sub-microscale increases significantly. A small portion of the larger reinforcements derives from originally larger Ti powders, while the majority of these should result from the growth of nano-reinforcing particulates through mergence, as indicated

by the arrows in Fig. 4(e), (f), (i), (j), (m) and (n), since higher fraction of reinforcing particulates provides more chances for the nano-reinforcing particulates to touch with each other. In addition, the nature of different reinforcing particulates is determined by means of high-resolution TEM and electron diffraction patterns [Fig. 5(a)–(i)]. As is seen, the nano-particulates, submicron-particulates and the Al–Ti intermetallic shell of micro-CS particulates are all determined to be Al_3Ti phase from multiple zone axis of [001], $[1\bar{1}0]$, $[5\bar{1}1]$ and $[0\bar{6}1]$, rather than other intermetallic compounds in the Al–Ti binary system like AlTi , AlTi_3 or Al_2Ti [22]. Besides, the inset in Fig. 5(d) shows a good $\text{Al}_3\text{Ti}/\text{Al}$ interface condition.

According to the aforementioned microstructure observations, the size distributions of reinforcing particulates in 3%, 5%, 8% and 10% Ti_p AMCs are determined. The results, as displayed in Supplementary Fig. S2(a)–(d), demonstrate that the synthesized AMCs in this work all contain multiscale reinforcing particulates ranging widely from nanoscale to microscale. The particulates with size below $1\ \mu\text{m}$ account for most reinforcements in frequency. Overall, the reinforcing particulates synthesized in 3%, 5%, 8% and 10% Ti_p AMCs have a M&D architecture.

Tensile properties and comparisons

The tensile properties of 3%, 5%, 8% and 10% Ti_p AMCs are displayed in Fig. 6(a), and those of pure Al are also included for the purpose of comparison. The yield strength (σ_y), ultimate tensile strength (σ_u) and elongation to failure (ϵ_f) of pure Al are 135 MPa, 158 MPa and 23.1%, respectively. As the fraction of added M&D reinforcing particulates increases, the σ_y and σ_u are elevated significantly, and more fraction of reinforcements leads to higher tensile strengths. However, the ϵ_f first increases from 3 to 5% Ti_p AMCs and then decreases afterwards. The best toughening effect is achieved in the 5% Ti_p AMCs, at which the increments of σ_u and σ_y are as high as 66.5% and 66.7%, respectively, and at the same time a high ϵ_f nearly comparable to pure Al is retained. Figure 6(b) compares the work-hardening rate [$\Theta = \left(\frac{\partial\sigma}{\partial\epsilon}\right)_\epsilon$, σ : true stress, ϵ : true strain] of the AMCs reinforced by different fraction of M&D reinforcing particulates (AMCs-M&D). Apparently, higher fraction of M&D reinforcing particulates leads to higher Θ at the initial strain stage ($\epsilon < 2.5\%$), which indicates the strong interaction between M&D particulates and dislocations during tensile deformation.

To highlight the toughening merits of M&D particulates, we compared the relative strength increment η , which is defined as $\eta = (\sigma_{u\text{-AMCs}} - \sigma_{u\text{-Matrix}}) / \sigma_{u\text{-Matrix}}$ ($\sigma_{u\text{-AMCs}}$: ultimate tensile strength of AMCs, $\sigma_{u\text{-Matrix}}$: ultimate tensile strength of matrix), versus tensile ductility of AMCs reinforced by M&D particulates with those by CS (core: Al, shell: Al_3Ti) particulates [11, 15, 23] or monolithic Al_3Ti particulates [11, 24, 25] from the literatures. The results, as shown in Fig. 6(c), clearly demonstrate that

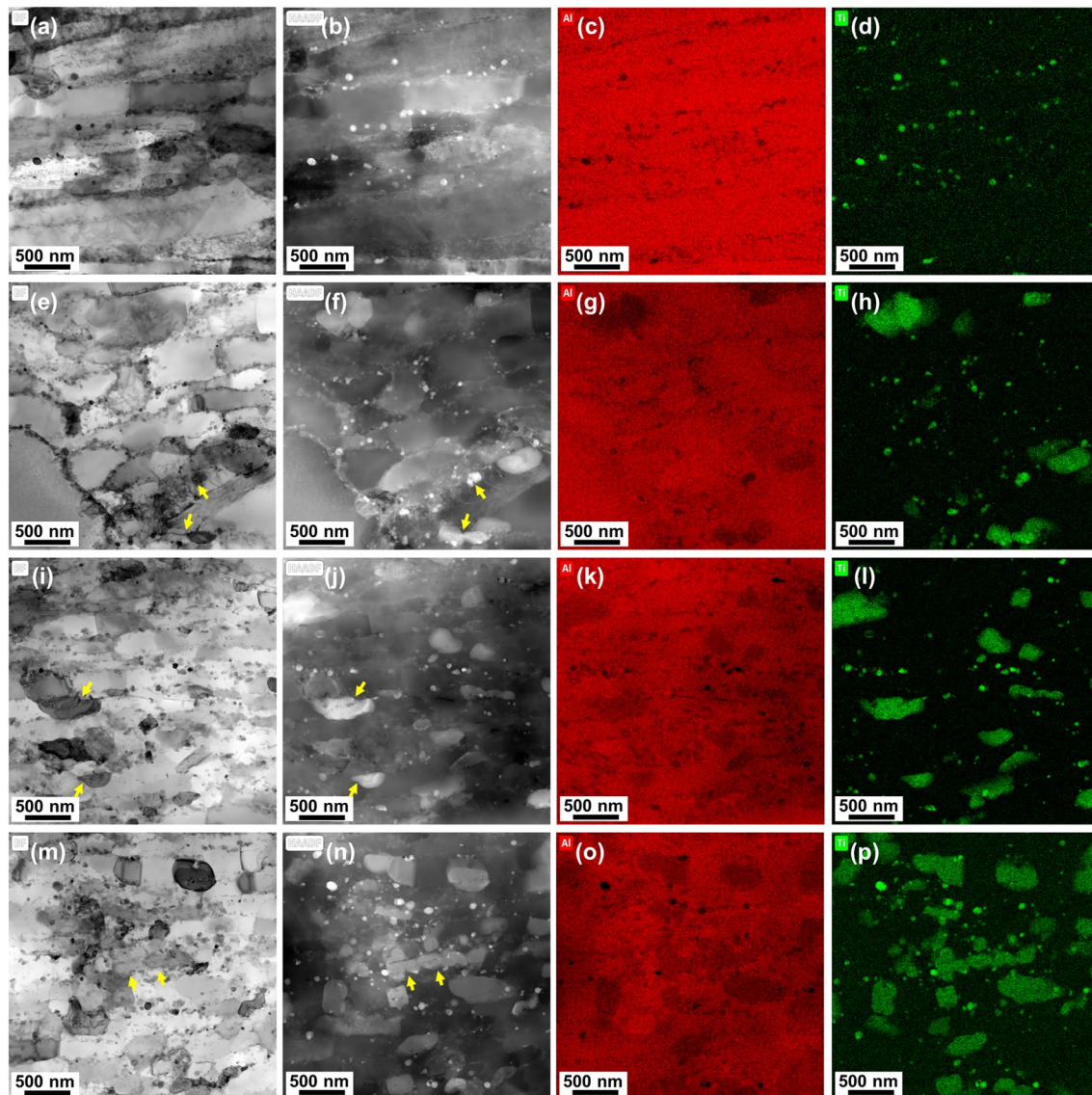


Figure 4: TEM (a, e, i, m) bright field, (b, f, j, n) high-angle annular dark field, EDS elemental mapping of (c, g, k, o) Al and (d, h, l, p) Ti elements in (a, b, c, d) 3%, (e, f, g, h) 5%, (i, j, k, l) 8% and (m, n, o, p) 10% Ti_p AMCs.

the M&D particulates exhibit a comparably high strengthening effect while retaining a decent ductility, i.e., a much better effect of toughening. The corresponding strengthening and toughening mechanisms will be presented in detail in what follows.

Discussion

Strengthening mechanisms

As is well-known, the strengthening of metallic materials comes mainly from the dislocations with their motions being impeded by second-phase particle, solute atom, twin boundary, grain boundary, etc. [26, 27]. Our discussion on the strengthening mechanisms of M&D reinforcing particulates begins from the ones with smaller size. The strength increment at such scale

results mainly from Orowan strengthening [28] that is caused by dislocation bypassing nano-particulates, as shown in Fig. 7(a) and (b), in which the interaction between nano-particulates and dislocations can be clearly observed. The Orowan strengthening mechanism is only effective for the reinforcing particulates with smaller size, generally less than $1 \mu\text{m}$ [29], as the shear stress for the dislocation to bypass particulates with larger size scales up greatly. Therefore, the effects of nano- and submicro-particulates are only considered for the Orowan strengthening mechanism. Here Eq. (1) is used to calculate the yield strength increment from the Orowan strengthening (σ_{OR}) [30]:

$$\sigma_{OR} = M \cdot \frac{0.81Gb}{2\pi(1-\nu)^{1/2}\lambda} \ln\left(2\sqrt{2/3}r_{n\&s}/r_0\right), \quad (1)$$

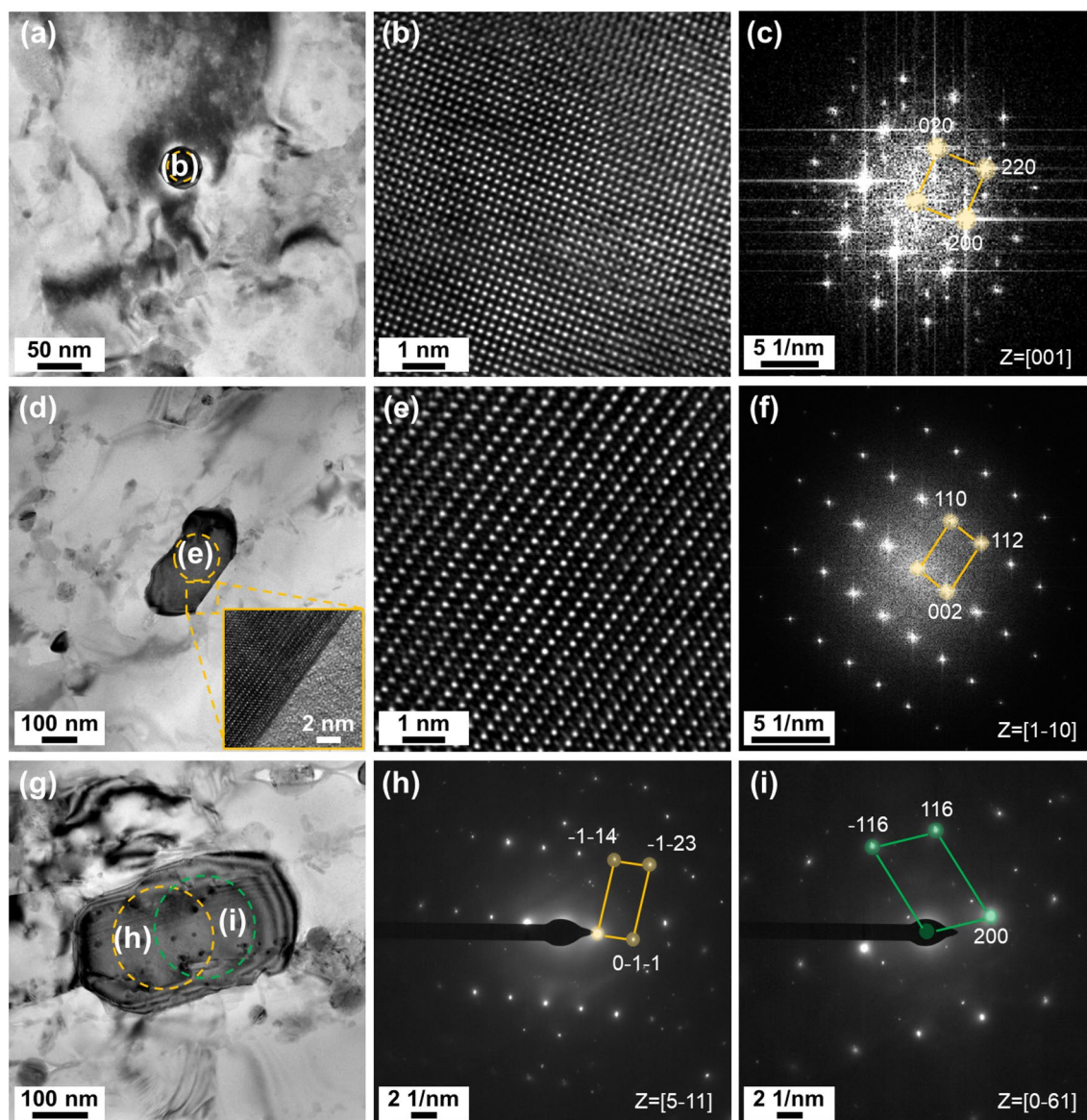


Figure 5: TEM characterization of (a–c) nano-particulates and (d–i) submicro-particulates: (a, d, g) bright field images, (b, e) high-resolution TEM images of the circled areas in (a, d) and (c, f) corresponding Fast Fourier transform images, (h, i) selected area diffraction patterns of the area marked in (g) by titling the same particulate into different zone axis. Note that the inset in (d) shows the particulate/matrix interface condition.

where G is the shear modulus of Al matrix (25.6 GPa [29]), ν is the Poisson ratio (0.33 [31]), M is the Taylor factor (3 [30]), b is the Burgers vector (0.28 nm [29]), $r_{n\&s}$ is the mean radius of the nano- and submicro-particulates, r_0 is the dislocation core radius ($r_0 = 4b$), λ is the interparticle spacing that can be obtained by the following equation [30]:

$$\lambda = \sqrt{2/3} \left[1.25 \sqrt{\pi/V_{n\&s}} - 2 \right] r_{n\&s}, \quad (2)$$

where $V_{n\&s}$ is the statistical volume fraction of the nano- and submicro-particulates, which is 0.064%, 0.10%, 0.33% and 0.65% for 3%, 5%, 8% and 10% Ti_p AMCs, respectively. As a result, the

strength increments from Orowan strengthening on 3%, 5%, 8% and 10% Ti_p AMCs are calculated to be 3.01 MPa, 3.22 MPa, 3.76 MPa and 4.87 MPa, respectively.

Due to the difference between coefficient of thermal expansion (CTE) of Al_3Ti ($11.9 \times 10^{-6} K^{-1}$) and Al ($23.6 \times 10^{-6} K^{-1}$) [15], dislocations could be generated around Al matrix adjacent to Al_3Ti particulates, especially for those at submicro and micro scale. These dislocations can act as obstacles for the subsequent mobile dislocations, which is known as CTE mismatch strengthening [32]. The strength increment resulting from CTE mismatch strengthening (σ_{CTE}) can be quantified through the following equation [15]:

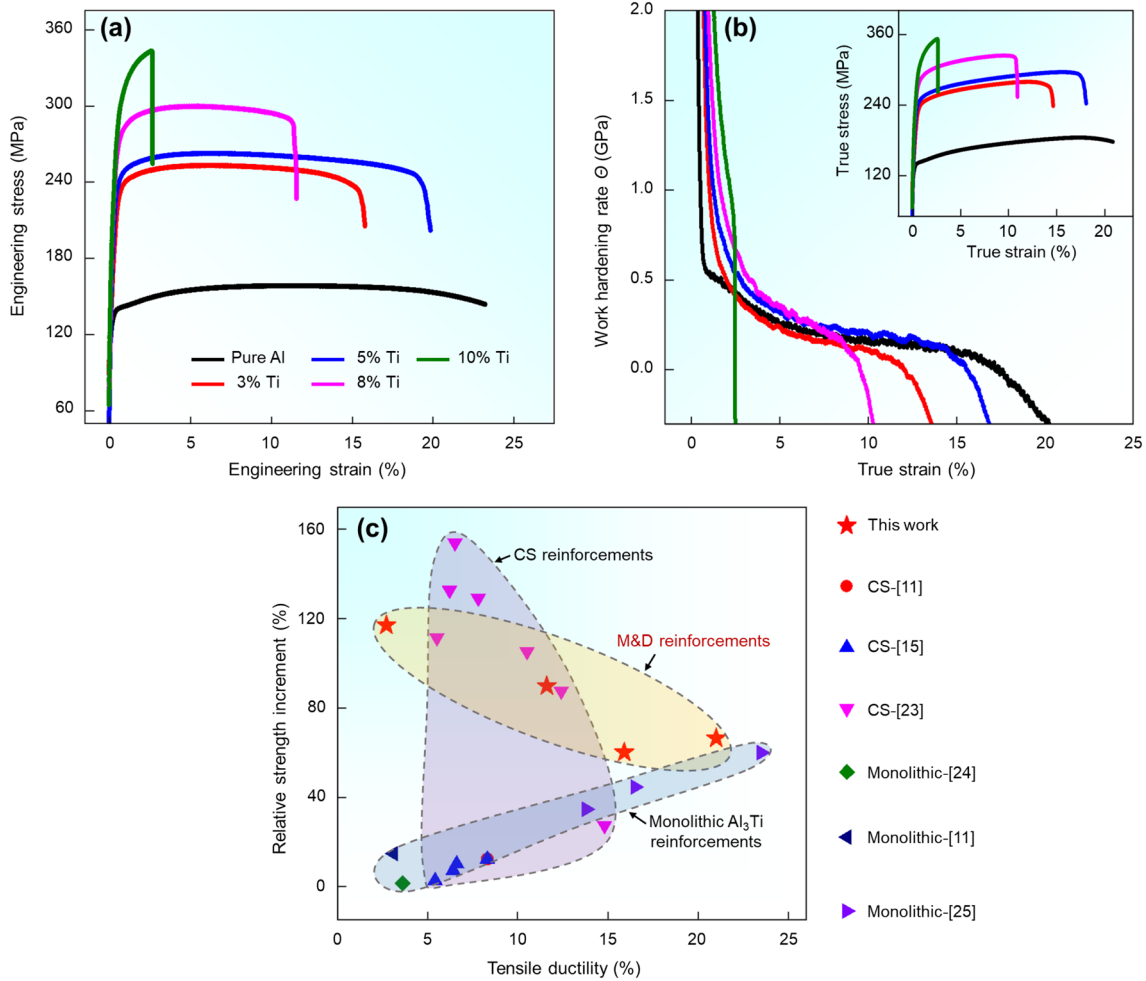


Figure 6: Tensile properties of AMCs reinforced with multiscale and dual-structured reinforcing particulates and pure Al: (a) typical engineering strain–stress curves, (b) plots of work hardening rate (Θ) versus true stress (σ) with the inset showing corresponding true strain–stress curves, and (c) comparison of relative strength increment versus tensile ductility of AMCs reinforced by CS particulates (core: Al, shell: Al_3Ti) and monolithic Al_3Ti particulates [11, 15, 23–25] with M&D particulates in this work.

$$\sigma_{\text{CTE}} = \alpha Gb \left(\frac{12\Delta T \Delta C V_{\text{M\&D}}}{bd_{\text{M\&D}}(1 - V_{\text{M\&D}})} \right)^{1/2}, \quad (3)$$

where α is a constant (1 [33]), ΔT is the temperature change (615 K), ΔC is the difference in CTE between Al_3Ti and Al ($11.7 \times 10^{-6} \text{ K}^{-1}$), $V_{\text{M\&D}}$ is the volume fraction of the M&D reinforcing particulates, which is 5%, 7%, 10% and 16% for 3%, 5%, 8% and 10% Ti_p AMCs, respectively, $d_{\text{M\&D}}$ is the mean size of the M&D reinforcing particulates, which is 0.88 μm , 1.04 μm , 0.96 μm and 0.96 μm for 3%, 5%, 8% and 10% Ti_p AMCs, respectively. The strength increments from CTE mismatch strengthening are 30.78 MPa, 33.86 MPa, 42.82 MPa and 56.07 MPa for the 3%, 5%, 8% and 10% Ti_p AMCs, respectively.

Another strengthening mechanism is the strength increment resulting from geometrically necessary dislocations (GNDs) generated at the Al matrix adjacent to the M&D particulates. During tensile testing, first deformation occurs in

the soft Al matrix and the rigid M&D particulates deforms subsequently when enough stress is accumulated, which engender GNDs at the side of Al matrix to accommodate the strain incompatibility between these two phases, as indicated by Fig. 7(c) and (d). The formation of GNDs can not only avoid the early fracture of AMCs by facilitating the strain partitioning between M&D particulates and Al matrix, but also contribute to the strengthening. As for the M&D reinforcements in this work, all the particulates are likely to generate GNDs, and the strength increment from the GNDs strengthening (σ_{GNDs}) could be obtained through the following equation [34]:

$$\sigma_{\text{GNDs}} = \frac{2G(1 - \nu)V_{\text{M\&D}}\epsilon}{1 - 2\nu}, \quad (4)$$

where ϵ is the yield strain of the alloy (0.002). The strength increments from GNDs strengthening on 3%, 5%, 8% and 10% Ti_p

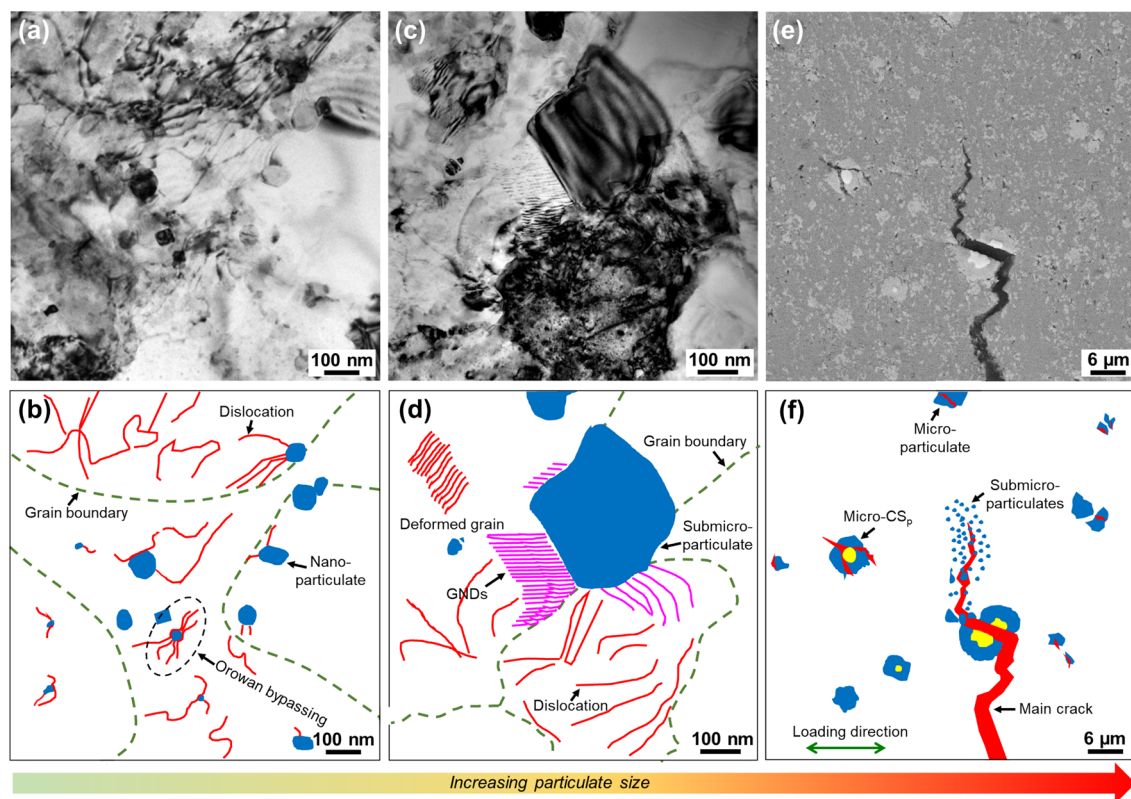


Figure 7: (a, c, e) Deformation behaviors and (b, d, f) schematic drawings showing different strengthening mechanisms of (a) nano-particles, (b) submicro-particles and (c) micro-CS particulates.

AMCs are calculated to be 6.56 MPa, 9.18 MPa, 13.12 MPa and 20.99 MPa, respectively.

In addition, the role of M&D particulates, especially those at the microscale level, stands out when the crack advances. As exhibited in Fig. 7(e) and (f), the reinforcing particulates ahead of the crack tip fracture earlier owing to much higher stress field ahead of crack tips than anywhere else [11]. This indicates that the reinforcing particulates sustain tensile stress transferred from the Al matrix and give rise to strengthening from the well-known load transfer mechanism, which can be described as [35]:

$$\sigma_{LD} = \sigma_m \left[\frac{V_{M\&D}(S + 2)}{2} + V_m \right], \quad (5)$$

where σ_{LD} is the yield strength increment induced by load transfer mechanism, σ_m is the yield strength of Al matrix, S is the aspect ratio of the reinforcing particulates, here referring to the M&D particulates at all scales as this strengthening mechanism can also take place in smaller ones; V_m is the volume fraction of the Al matrix. Under this condition, the strength increments from load transfer mechanism on 3%, 5%, 8% and 10% Ti_p AMCs are quantified to be 138.71 MPa, 141.14 MPa, 145.80 MPa and 153.36 MPa, respectively.

Besides, as the Ti powders were added into the Al matrix, a small fraction of Ti element would dissolve into the Al matrix

to form supersaturated solid solution, as shown in Fig. 8(a) and (b). The yield strength increment resulting from solid solution strengthening (σ_{SS}) can be obtained by Eq. (6) [36]:

$$\sigma_{SS} = G\epsilon' \sqrt{x_f/4}, \quad (6)$$

where x_f is the concentration of the Ti solute atom, which are 0.11 at.%, 0.13 at.%, 0.22 at.% and 0.29 at.%, as determined by EDS spot analysis equipped on TEM, for the 3%, 5%, 8% and 10% Ti_p AMCs; ϵ' is the fractional difference between the diameter of Al atom and Ti solute atom (0.0391 [15]). The strength increments from solid solution strengthening on 3%, 5%, 8% and 10% Ti_p AMCs are calculated to be 16.60 MPa, 18.05 MPa, 23.47 MPa and 26.95 MPa, respectively.

Furthermore, the existence of M&D reinforcing particulates decreases the grain size of Al matrix to a large degree (Fig. 3), which multiplies the number of grain boundaries per unit volume. As shown in Fig. 8(c) and (d), the grain boundary is an effective barrier for dislocation motion and thus the effect of grain boundary strengthening has to be taken into account. The yield strength increment from grain boundary strengthening (σ_{GB}) can be quantified by the well-known Hall–Petch equation [37–39]:

$$\sigma_{GB} = k/\sqrt{d}, \quad (7)$$

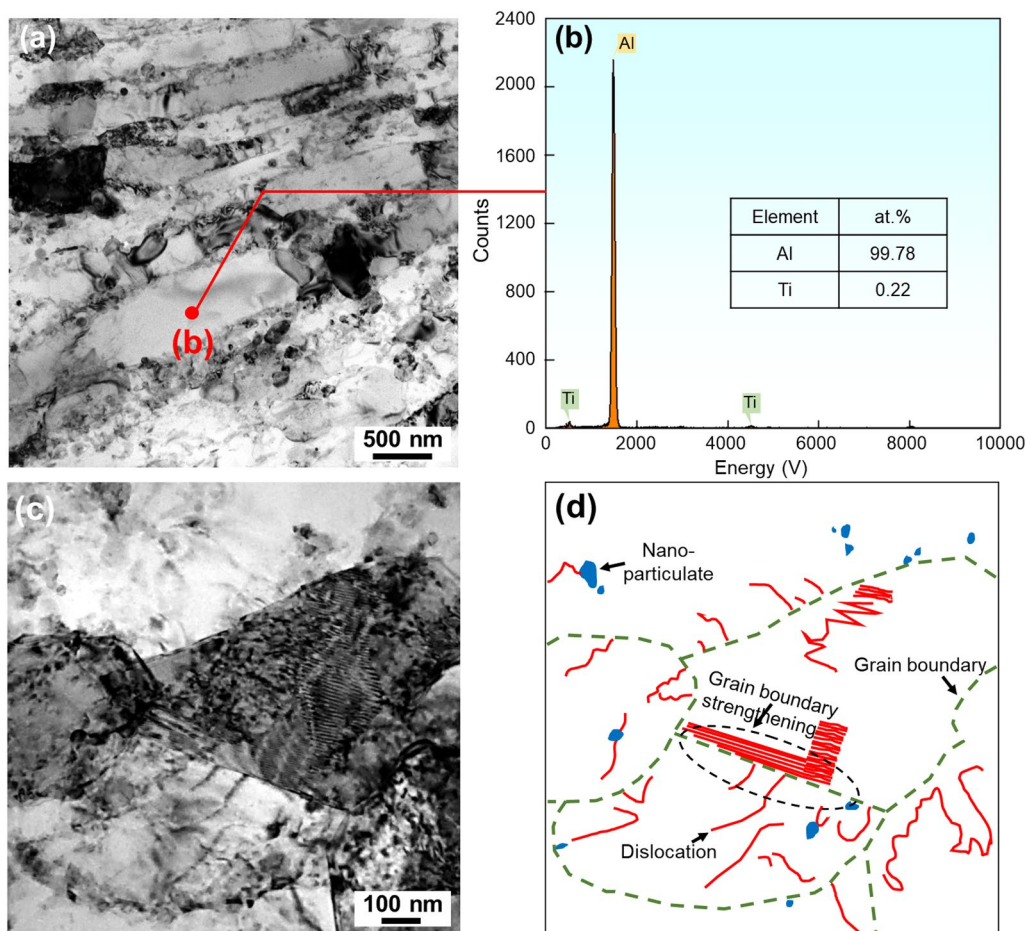


Figure 8: (a) TEM bright field image of AMCs-M&D, (b) EDS spot analysis results of Al grain marked with identical letter in (a), (c) TEM bright field image showing deformed Al grains in AMCs-M&D, and (d) schematic drawing showing grain boundary strengthening.

where k is the Hall–Petch slope ($0.07 \text{ M N}\cdot\text{m}^{-3/2}$ [40]), d is the average grain size of Al matrix in AMCs-M&D. The strength increments from grain boundary strengthening on 3%, 5%, 8% and 10% Ti_p AMCs are calculated to be 79.26 MPa, 81.93 MPa, 82.50 MPa and 83.67 MPa, respectively.

It can be concluded from the above calculations that the load transfer mechanism contributes most increment to the overall yield strength, which is followed by grain boundary strengthening and CTE mismatch strengthening. The strength increments from Orowan strengthening, GNDs strengthening and solid solution strengthening are the least. We also predict the overall yield strength of AMCs-M&D via the strength increments from above strengthening mechanisms. Arithmetic addition can be used to estimate the upper bound of theoretical yield strength of AMCs-M&D ($\sigma_{\text{AMCs-M\&D}}$) by considering these five strengthening mechanisms: $\sigma_{\text{AMCs-M\&D}} = \sigma_{\text{OR}} + \sigma_{\text{CTE}} + \sigma_{\text{GNDs}} + \sigma_{\text{LD}} + \sigma_{\text{SS}} + \sigma_{\text{GB}}$, which are 274.93 MPa, 287.38 MPa, 311.47 MPa and 345.91 MPa for 3%, 5%, 8% and 10% Ti_p AMCs, respectively. Although the predicted yield strengths are somewhat higher than the

experimental ones due likely to the existence of voids, the gradual increase in theoretical yield strength with particulate fraction agrees well with the experimental one, i.e., the variation trend is successfully predicted.

Toughening mechanisms

The above results on the work hardening behaviors of AMCs-M&D reveal that enhanced work hardening rate can be achieved by higher fraction of M&D particulates especially at the initial strain stage [Fig. 6(b)], and high work hardening rate is actually a prerequisite for achieving simultaneously high strength and high ductility in metallic materials [11, 41]. To probe into the work hardening-related toughening mechanisms, the post-deformation microstructures of AMCs-M&D were examined firstly by TEM. As shown in Fig. 9(a)–(d), the dislocation activities around the nano- Al_3Ti particulates (labelled by numbers ①–④) are much more conspicuous than anywhere else of this grain, that is, the dislocations that prevails in the grain are mainly concentrated around the nano- Al_3Ti particulates. The

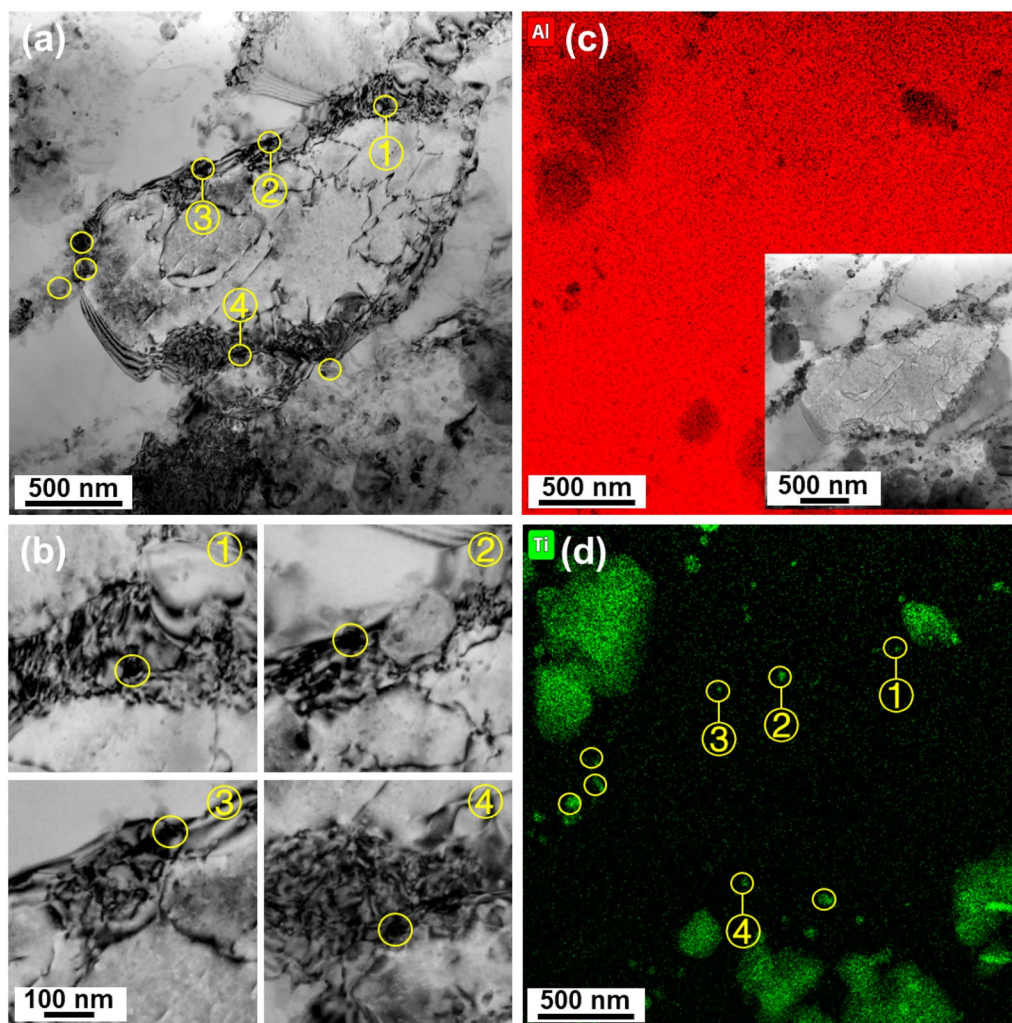


Figure 9: Post-deformation microstructures of AMCs-M&D after tensile testing: (a) TEM bright-field image, (b) magnified details of areas ①–④ circled in (a) with identical numbers; EDS elemental mapping of (c) Al and (d) Ti elements with the insets in (c) showing the corresponding TEM image from which the EDS analysis was performed.

possible reasons, on one hand, are the impeding effect of nano-particulates against the movement of dislocations propagated from the grain interior, which forms dislocation tangles around the reinforcing particulates [11, 42, 43]. On the other hand, the nano- Al_3Ti particulates might serve as sources to emit dislocations. Generally, a high critical stress is required for dislocation nucleation due to its energy barrier [44]. But the moderate lattice mismatch at the particulate/matrix interface can give rise to a stress concentration, which lower the energy barrier for dislocation nucleation [45]. In this case, the required stress to emit dislocations at the interface with a lattice mismatch is comparably lower, making it possible to achieve sustainable dislocation nucleation from a particulate [46]. The relationship between the Al_3Ti particulate and Al matrix synthesized in this work can meet these requirements well by forming a coherent interface with a small lattice mismatch between $\text{Al}_3\text{Ti}/\text{Al}$ interface

($\epsilon_{aa} = +4.83\%$, $\epsilon_{cc} = -5.99\%$ [19]). However, as the radius of particulate increases, the stress demanded for dislocation nucleation becomes higher as a result of much greater energy barrier [44]. Therefore, during plastic deformation the sustainable dislocations are first emitted from nano- Al_3Ti particulates at high stress, which are supported by the post-deformed TEM observations in our previous article [19]. The emission of dislocations from nano- Al_3Ti particulates aggravates the dislocation concentration around the reinforcements. Therefore, the impeding of dislocations or emitting dislocations by nano-particulates enhance the work hardening of M&D particulate reinforced AMCs greatly, which is beneficial for toughening.

As for the CS particulates at the microscale, peculiar fracture behaviors differing from the conventional monolithic particulates were observed. As displayed in Fig. 10(a)–(c), crack forms firstly in the intermetallic shell (indicated by number ①)

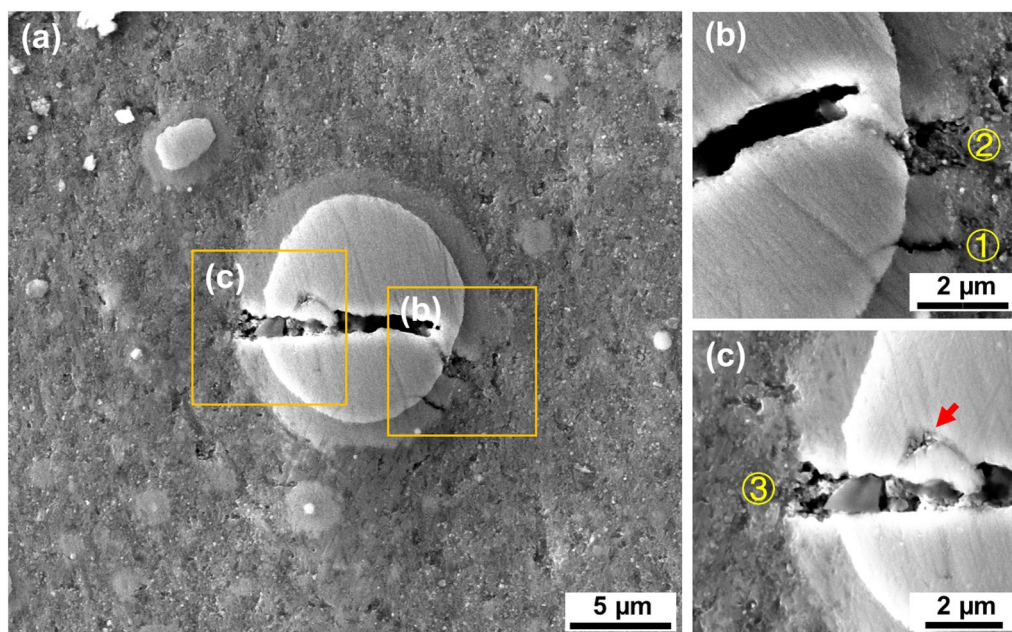


Figure 10: (a) SEM image showing deformed microstructures of micro-CS particulates, (b) and (c) are the magnified views of the square areas in (a).

due to its much higher hardness (~4.5 GPa [11]) than those of Ti core (1.84 GPa [11]) and surrounding Al matrix (~1.69 GPa [11]). With increasing the external tensile stress, the crack would propagate into the two sides of inner Ti core and outer Al matrix (indicated by number ②). As the hcp-Ti is less ductile than the fcc-Al, the crack then penetrates through the entire Ti core (indicated by number ③) accompanied with the formation of bifurcation (indicated by arrow), at which moment the CS reinforcing particulates fail totally and then the crack starts to propagate into the Al matrix. Such successive failure from the outside hard shell to inside soft Ti core can not only reduce the initially formed crack size by constraining it in thin shell and thus delay crack propagation [19], but also consume tensile energy and improve the fracture resistance, which increases the toughness of AMCs-M&D significantly, as proved by finite element modeling simulation in another composite system [11]. Overall, the enhanced work hardening rate resulting from nano-particulates' impeding dislocation motion or emitting dislocations as well as the successive fracture of micro-CS particulates from the outer shell to inner Ti core accounts for the toughening mechanisms of M&D reinforcing particulates.

Based on the above, the possible reasons for the variations in ductility with M&D reinforcing particulates are then presented in the following. The nano-particulates and micro-CS particulates are beneficial for improving ductility by emitting dislocations and successive fracture, respectively. As the fraction of added Ti_p increases, the fraction of formed M&D reinforcing particulates increases and so does the total fraction of nano-particulates and micro-CS particulates. In this way the ductility of AMCs is gradually enhanced with increasing Ti_p from 3%

to 5%. However, the submicro-particulates are detrimental to the ductility of AMCs by accumulating stress concentration at the Al_3Ti/Al interface and then failing first during deformation. Unfortunately, as evidenced in Fig. 4, when the Ti_p is increased to 8% and 10%, the proportion of reinforcements at sub-micro-scale increases significantly, which results from the growth of nano-reinforcing particulates through merrgence since higher fraction of reinforcing particulates provides more chances for the nano-reinforcing particulates to touch with each other, as stated above. That is, when the fraction of Ti_p exceeds 5%, the harmful effect from increased submicro-particulates on ductility aggravates more obviously than the beneficial effect from increased nano-particulates and micro-CS particulates. In this case the ductility of AMCs decreases gradually with further increasing Ti_p to 8% and 10%.

Conclusions

The following conclusions can be drawn:

- (1) M&D reinforcing particulates that are composed of nano-/submicro- Al_3Ti reinforcing particulates with monolithic structure and micro-CS reinforcing particulates with inner Ti core and outer Al_3Ti intermetallic shell are distributed uniformly in the AMCs.
- (2) An increase in the fraction of M&D reinforcing particulates decreases the grain size of Al matrix due to the impeding of reinforcing particulates against the disappearance of grain boundary, and there's no distinct preferred grain orientation in the AMCs.

- (3) As the fraction of M&D reinforcing particulates increases, the yield strength and ultimate tensile strength increase significantly. However, the tensile elongation first increases from 3% to 5% Ti_p AMCs and then decreases afterwards. The best toughening effect is achieved in the 5% Ti_p AMCs, at which the increments of ultimate tensile strength and yield strength are as high as 66.5% and 66.7%, respectively, and simultaneously a high elongation nearly comparable to pure Al is retained. The M&D particulates exhibit a much better effect of toughening than CS or monolithic particulates.
- (4) The strength increments from load transfer mechanism are the largest, which is followed by grain boundary strengthening and CTE mismatch strengthening, the strength increments from Orowan strengthening, GNDs strengthening and solid solution strengthening are the least.
- (5) The enhanced work-hardening rate resulting from nano-particulates' impeding dislocation motion or emitting dislocations as well as the successive fracture of micro-CS particulates from the outer shell to inner Ti core accounts for the toughening mechanisms of M&D reinforcing particulates.

Experimental procedure

Pure Al was selected as the matrix so as to remove the effect from solute elements. Both the in situ formed monolithic particulates and CS particulate are achieved through the reaction between pure Al and pure Ti in varied size. To meet these requirements, pure Al powders with 99.99% in purity and ~1 μm in mean size [Supplementary Fig. S3(a)] as well as pure Ti powders with 99.99% in purity and 2 nm to 4 μm in size distribution [Supplementary Fig. S3(b)] were utilized in this work.

To clarify the effect of reinforcement fraction on the composites, 3%, 5%, 8% and 10% (in weight fraction) pure Ti powders were mixed with 97%, 95%, 92% and 90% (in weight fraction) pure Al powders in a planetary ball-milling machine to fabricate 3%, 5%, 8% and 10% Ti particulate-reinforced (Ti_p) AMCs. The vacuum pressure machine was used to compact the powder mixtures with the temperature of 300 °C, holding time of 30 min and pressure of 277 MPa. Subsequently, the tubular vacuum resistance furnace was utilized to heat the compressed billets, which lasted for 40 min under 640 °C to induce the Ti/Al reaction. Then, the heated billets were quickly placed to a die cavity preheated to 250 °C and finally forged under 150 MPa for 20 s. The reference material of pure Al was also processed with the same procedures.

Microstructural characterizations were performed on specimen with size of 20 mm × 10 mm × 10 mm, which was taken from the central parts of each thixoforged sample. QUANTA

FEG 450 scanning electron microscope (SEM) equipped with electron backscattered diffraction (EBSD) detector was used for microstructural observations at the submicro- and micro-scale. A step size of 100 nm was used for EBSD analysis. EPMA-1600 electron probe microanalyzer was utilized for analyze element distributions in the synthesized AMCs with varied reinforcement fraction. FEI Talos F200X equipped with Super-X energy disperse spectroscopy (EDS) operated at 200 kV was used for TEM characterization, i.e., bright field imaging, high-angle annular dark-field (HAADF) imaging and EDS analysis. The latter two were conducted under a scanning transmission electron microscopic (STEM) mode. Room-temperature tensile test was implemented under a strain rate of 10⁻³ s⁻¹ utilizing an extensometer, and the mean value of three tests was taken as the final properties. The preparation details for tensile test specimens were given elsewhere [19].

Acknowledgments

This research was supported by Zhejiang Provincial Natural Science Foundation of China under Grant No. LQ22E010006, Science and Technology Program of Gansu Province under Grant No. 21JR7RA257, Gansu Provincial Department of Education: Innovation Fund Project under Grant No. 2022A-024, and Support Program for Hongliu Excellent Young Talents of Lanzhou University of Technology.

Author contributions

XZ: Conceptualization, Methodology, Formal Analysis, Data Curation, Writing—Original Draft, Writing—Review and Editing, Project Administration, Funding Acquisition. WL: Investigation. TC: Supervision.

Data availability

The data that support the findings of this study are available from the corresponding author upon reasonable request.

Declarations

Conflict of interest The authors declare that they have no known competing financial interests or personal relationships that could have appeared to influence the work reported in this paper.

Supplementary Information

The online version contains supplementary material available at <https://doi.org/10.1557/s43578-023-01128-0>.

References

1. D.J. Lloyd, Particle reinforced aluminium and magnesium matrix composites. *Metall. Rev.* **39**(1), 1 (1994)

2. I.A. Ibrahim, F.A. Mohamed, E.J. Lavernia, Particulate reinforced metal matrix composites—a review. *J. Mater. Sci.* **26**(5), 1137 (1991)
3. J.W. Kaczmar, K. Pietrzak, W. Włosiński, The production and application of metal matrix composite materials. *J. Mater. Process. Technol.* **106**(1), 58 (2000)
4. P.S. Bains, S.S. Sidhu, H. Payal, Fabrication and machining of metal matrix composites: a review. *Mater. Manuf. Process.* **31**(5), 553 (2016)
5. A. Mortensen, I. Jin, Solidification processing of metal matrix composites. *Int. Mater. Rev.* **37**(1), 101 (1992)
6. P. Rohatgi, R. Asthana, S. Das, Solidification, structures, and properties of cast metal–ceramic particle composites. *Int. Met. Rev.* **31**(1), 115 (1986)
7. M. Song, D. Huang, Experimental and modeling of the coupled influences of variously sized particles on the tensile ductility of SiC_p/Al metal matrix composites. *Metall. Mater. Trans. A* **38**(9), 2127 (2007)
8. V.A. Romanova, R.R. Balokhonov, S. Schmauder, The influence of the reinforcing particle shape and interface strength on the fracture behavior of a metal matrix composite. *Acta Mater.* **57**(1), 97 (2009)
9. M. Geni, M. Kikuchi, Damage analysis of aluminum matrix composite considering non-uniform distribution of SiC particles. *Mech. Eng.* **46**(9), 3125 (2002)
10. I. Sabirov, O. Kolednik, R.Z. Valiev, R. Pippan, Equal channel angular pressing of metal matrix composites: effect on particle distribution and fracture toughness. *Acta Mater.* **53**(18), 4919 (2005)
11. X. Zhang, T. Chen, S. Ma, H. Qin, J. Ma, Overcoming the strength–ductility trade-off of an aluminum matrix composite by novel core–shell structured reinforcing particulates. *Composites B* **206**, 108541 (2021)
12. C.J. Hsu, C.Y. Chang, P.W. Kao, N.J. Ho, C.P. Chang, Al–Al₃Ti nanocomposites produced in situ by friction stir processing. *Acta Mater.* **54**(19), 5241 (2006)
13. A. Olszówka-Myalska, Microstructural study of the aluminium/nickel aluminide interface formed in a hot-pressed in situ composite. *Mater. Chem. Phys.* **81**(2), 333 (2003)
14. I.S. Lee, P.W. Kao, N.J. Ho, Microstructure and mechanical properties of Al–Fe in situ nanocomposite produced by friction stir processing. *Intermetallics* **16**(9), 1104 (2008)
15. T.J. Chen, H. Qin, X.Z. Zhang, Effects of reheating duration on the microstructure and tensile properties of in situ core–shell-structured particle-reinforced A356 composites fabricated via powder thixoforming. *J. Mater. Sci.* **53**(Suppl 2), 2576 (2018)
16. Y. Wang, M. Song, S. Ni, Y. Xue, In situ formed core–shell structured particle reinforced aluminum matrix composites. *Mater. Des.* **56**(4), 405 (2014)
17. Y. Xue, R. Shen, S. Ni, M. Song, D. Xiao, Fabrication, microstructure and mechanical properties of Al–Fe intermetallic particle reinforced Al-based composites. *J. Alloys Compds* **618**, 537 (2015)
18. J.Y. Zhang, T.J. Chen, X.Z. Zhang, M. Gao, L.B. Geng, Simultaneously strengthening and toughening a core–shell structured particulate reinforced aluminum alloy-based composite by solid solution treatment. *J. Alloys Compds* **842**, 155765 (2020)
19. X. Zhang, W. Lu, T. Chen, Multiscale and dual-structured reinforcing particulates enhance the strength of aluminum matrix composites at no ductility loss. *Mater. Sci. Eng. A* **856**, 144003 (2022)
20. H. Meng, X. Chao, G. Fan, E. Maawad, W. Gan, G. Lin, F. Lin, G. Tang, W. Hao, D. Yan, Role of layered structure in ductility improvement of layered Ti–Al metal composite. *Acta Mater.* **153**, 235 (2018)
21. M. Ipekoglu, A. Nekouyan, O. Albayrak, S. Altintas, Mechanical characterization of B₄C reinforced aluminum matrix composites produced by squeeze casting. *J. Mater. Res.* **32**(3), 599 (2017)
22. Y.J. Wang, T.J. Chen, S.Q. Zhang, Y.H. Qin, X.Z. Zhang, Effects of partial remelting on microstructure of Al–Si–Ti bulk alloy prepared by cold pressing mixed powders. *Mater. Trans.* **57**(7), 1124 (2016)
23. A. Rezaei, H.R. Madaah Hosseini, Evolution of microstructure and mechanical properties of Al–5 wt% Ti composite fabricated by P/M and hot extrusion: effect of heat treatment. *Mater. Sci. Eng. A* **689**, 166 (2017)
24. S. Ma, X. Wang, Mechanical properties and fracture of in situ Al₃Ti particulate reinforced A356 composites. *Mater. Sci. Eng. A* **754**, 46 (2019)
25. R. Gupta, G.P. Chaudhari, B.S.S. Daniel, Strengthening mechanisms in ultrasonically processed aluminium matrix composite with in situ Al₃Ti by salt addition. *Composites B* **140**, 27 (2018)
26. L. Sun, G. Wu, Q. Wang, J. Lu, Nanostructural metallic materials: structures and mechanical properties. *Mater. Today* **38**, 114 (2020)
27. D. Zhang, Ultrafine grained metals and metal matrix nanocomposites fabricated by powder processing and thermomechanical powder consolidation. *Prog. Mater. Sci.* **123**, 100853 (2022)
28. B. Guo, M. Song, X. Zhang, Y. Liu, X. Cen, B. Chen, W. Li, Exploiting the synergic strengthening effects of stacking faults in carbon nanotubes reinforced aluminum matrix composites for enhanced mechanical properties. *Composites B* **211**, 108646 (2021)
29. X.Z. Zhang, T.J. Chen, Y.H. Qin, Effects of solution treatment on tensile properties and strengthening mechanisms of SiC_p/6061Al composites fabricated by powder thixoforming. *Mater. Des.* **99**, 182 (2016)
30. Q. Zhang, B.L. Xiao, W.G. Wang, Z.Y. Ma, Reactive mechanism and mechanical properties of in situ composites fabricated from an Al–TiO₂ system by friction stir processing. *Acta Mater.* **60**(20), 7090 (2012)

31. Z. Wang, J. Tan, B.A. Sun, S. Scudino, K.G. Prashanth, W.W. Zhang, Y.Y. Li, J. Eckert, Fabrication and mechanical properties of Al-based metal matrix composites reinforced with Mg₆₅Cu₂₀Zn₅Y₁₀ metallic glass particles. *Mater. Sci. Eng. A* **600**, 53 (2014)
32. R.J. Arsenault, N. Shi, Dislocation generation due to differences between the coefficients of thermal expansion. *Mater. Sci. Eng.* **81**, 175 (1986)
33. D. Poirier, R.A.L. Drew, M.L. Trudeau, R. Gauvin, Fabrication and properties of mechanically milled alumina/aluminum nanocomposites. *Mater. Sci. Eng. A* **527**(29), 7605 (2010)
34. M.F. Ashby, The deformation of plastically non-homogeneous materials. *Philos. Mag.* **21**(170), 399 (1970)
35. V.C. Nardone, K.M. Prewo, On the strength of discontinuous silicon carbide reinforced aluminum composites. *Scr. Metall.* **20**(1), 43 (1986)
36. X.C. Tong, A.K. Ghosh, Fabrication of in situ TiC reinforced aluminum matrix composites. *J. Mater. Sci.* **36**(16), 4059 (2001)
37. E.O. Hall, The deformation and ageing of mild steel: II. Characteristics of the Luders deformation. *Proc. Phys. Soc. B* **64**(9), 742 (1951)
38. N.J. Petch, The ductile-brittle transition in the fracture of α -iron: I. *Philos. Mag. J. Theor. Exp. Appl. Phys.* **3**(34), 1089 (1958)
39. H. Yang, S. Tian, T. Gao, J. Nie, Z. You, G. Liu, H. Wang, X. Liu, High-temperature mechanical properties of 2024 Al matrix nanocomposite reinforced by TiC network architecture. *Mater. Sci. Eng. A* **763**, 138121 (2019)
40. X.C. Tong, Fabrication of in situ TiC reinforced aluminum matrix composites Part I: microstructural characterization. *J. Mater. Sci.* **33**(22), 5365 (1998)
41. T. Wan, Z. Cheng, L. Bu, L. Lu, Work hardening discrepancy designing to strengthening gradient nanotwinned Cu. *Scr. Mater.* **201**, 113975 (2021)
42. Z. Lei, X. Liu, Y. Wu, H. Wang, S. Jiang, S. Wang, X. Hui, Y. Wu, B. Gault, P. Kontis, D. Raabe, L. Gu, Q. Zhang, H. Chen, H. Wang, J. Liu, K. An, Q. Zeng, T.-G. Nieh, Z. Lu, Enhanced strength and ductility in a high-entropy alloy via ordered oxygen complexes. *Nature* **563**(7732), 546 (2018)
43. K. Sang-Heon, K. Hansoo, N.J. Kim, Brittle intermetallic compound makes ultrastrong low-density steel with large ductility. *Nature* **518**(7537), 77 (2015)
44. S. Peng, Y. Wei, H. Gao, Nanoscale precipitates as sustainable dislocation sources for enhanced ductility and high strength. *Proc. Natl Acad. Sci. USA* **117**(10), 5204 (2020)
45. J. Li, B. Liu, Q. Fang, Z. Huang, Y. Liu, Atomic-scale strengthening mechanism of dislocation-obstacle interaction in silicon carbide particle-reinforced copper matrix nanocomposites. *Ceram. Int.* **43**(4), 3839 (2017)
46. H. Yang, K. Li, Y. Bu, J. Wu, Y. Fang, L. Meng, J. Liu, H. Wang, Nanoprecipitates induced dislocation pinning and multiplication strategy for designing high strength, plasticity and conductivity Cu alloys. *Scr. Mater.* **195**, 113741 (2021)

Publisher's Note Springer Nature remains neutral with regard to jurisdictional claims in published maps and institutional affiliations.

Springer Nature or its licensor (e.g. a society or other partner) holds exclusive rights to this article under a publishing agreement with the author(s) or other rightsholder(s); author self-archiving of the accepted manuscript version of this article is solely governed by the terms of such publishing agreement and applicable law.